Image reconstruction with uncertainty quantification in photoacoustic tomography

Jenni Tick[a)], Aki Pulkkinen, and Tanja Tarvainen[b)]
Department of Applied Physics,
University of Eastern Finland,
P.O.Box 1627,
70211 Kuopio, Finland

Running title: Photoacoustic tomography with uncertainty quantification.

Submitted: 23rd September 2015.

[a)]Electronic mail: jenni.tick@uef.fi
[b)]Also at Department of Computer Science, University College London, Gower Street, London WC1E 6BT, United Kingdom

Abstract

Photoacoustic tomography is a hybrid imaging method which combines optical contrast and ultrasound resolution. The goal of photoacoustic tomography is to resolve an initial pressure distribution from detected ultrasound waves generated within an object due to an illumination of a short light pulse. In this work, a Bayesian approach to photoacoustic tomography is described. The solution of the inverse problem is derived and computation of the point estimates for image reconstruction and uncertainty quantification is described. The approach is investigated with simulations in different detector geometries including limited view setup and with different detector properties such as ideal point-like detectors, finite size detectors, and detectors with a finite bandwidth. The results show that the Bayesian approach can be used to provide accurate estimates of the initial pressure distribution as well as information about the uncertainty of the estimates.

I. INTRODUCTION

Photoacoustic tomography (PAT), also known as optoacoustic tomography, is a hybrid imaging modality which combines optical contrast and high spatial resolution of ultrasound techniques. In PAT, a short (nanosecond scale) pulse of visible or near-infrared light is used to illuminate the region of tissue of interest. As light propagates within the tissue, it is absorbed by chromophores which are light absorbing molecules. The light absorption generates localized increases in pressure. The resulting pressure wave propagates through the tissue and is detected by ultrasound detectors on the surface of the object. In the inverse problem of PAT, the initial pressure distribution is reconstructed from the time-varying ultrasound measurements. PAT can provide structural, functional, and molecular information, and therefore it has a variety of biomedical applications. For reviews of physical principles of PAT, PAT image reconstruction, and its applications in biomedicine, see e.g. Refs. 1–5.

Several reconstruction algorithms have been utilized in the estimation of the initial pressure distribution. They can generally be categorized into eigenfunction expansion[6,7], backprojection[8–11], time reversal[12–14], and model-based image reconstruction algorithms[15–20]. In the eigenfunction expansion approach, the initial pressure is obtained as a series solution where the terms of the series are determined from the measured pressure signals. The backprojection algorithms are based on analytical inversion formulas, and they can be regarded as analogous with an (inverse) Radon transform e.g. in computed tomography (CT). The eigenfunction expansion and backprojection algorithms can provide exact reconstructions for certain geometries such as spherical, cylindrical and planar acoustic detection surfaces. However, the eigenfunction expansion and backprojection algorithms can not be utilized in arbitrary detector geometries. The time reversal algorithms are based on reciprocity principles in acoustics. In the approach, the initial pressure distribution is estimated by simulating ultrasound wave propagation backwards in time. The time reversal approach enables the image reconstructions in more general imaging scenarios than eigenfunction and backprojection approaches. However, the method has limitations in the case of open detector sets. The model-based image reconstruction algorithms are based on a discrete presentation of the acoustic model describing the propagation of sound. In the approach, the image reconstruction is performed by numerically minimizing the error between the measured acoustic signals and those computed using the acoustic model. Typically, the minimization problem is ill-posed, and therefore regularization such as Tikhonov regularization is utilized to stabilize the numerical inversion.

Generally, the above described methods and the reconstructed photoacoustic images are qualitative in the sense that they do not provide quantitative information on the parameters of interest. Furthermore, the uncertainties of the photoacoustic images are not typically assessed either.

In this paper, a Bayesian approach to PAT image reconstruction is proposed. In the Bayesian approach, all parameters are modeled as random variables[21–23]. A model describes how these parameters depend on each other, and information about the parameters is expressed by probability distributions. In the inverse problem, the idea is to obtain information about the parameters of primary interest based on the measurements, the model, and the prior information about the parameters. In principle, the distributions of the unknown parameters could be analyzed using Markov chain Monte Carlo (MCMC) methods. These
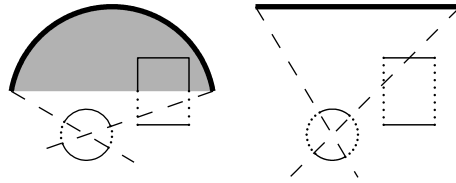
FIG. 1. Two examples of limited view imaging scenarios with detectors on an arc (left image) and on a line (right image). The region enclosed by the detectors (gray shaded area), the inclusion boundaries that are reconstructed accurately (solid line) and the inclusion boundaries that are blurred (dashed line). Image adapted from Refs. 3,29

methods, however, can be computationally prohibitively too expensive in large dimensional tomographic inverse problems. Therefore, point estimates, such as *maximum a posteriori* (MAP) estimate, are computed (image reconstruction). Furthermore, the reliability of the reconstructed images can be assessed by computing the credibilities of the estimates (uncertainty quantification).

The Bayesian approach has previously been utilized in image reconstruction in other light and/or ultrasound utilizing tomographic techniques in Refs. 24–28. However, to our knowledge, this is the first study in which the Bayesian approach to PAT is described. Furthermore, this is one of the few studies in which the uncertainties of the MAP estimates are evaluated in tomography.

In the case of 'an ideal' full view tomography, the object is fully surrounded by detectors on a closed surface. This, however, can not always be implemented in an experimental setting. The detector geometries which do not enclose the object are called limited view scenarios. It has been shown that, in limited view situations, the regions which are enclosed by the detection surface can be reconstructed accurately[29]. Those regions within the object, that are not enclosed by the detection surface, suffer from blurring apart from those inclusion boundaries whose normals intersect the detection surface[29]. The above conditions are illustrated in Fig. 1 where the area enclosed by the detectors is shaded with gray. The figure shows two inclusions inside the object. Those parts of the boundaries of the inclusions that can be estimated accurately are drawn with a solid line, and those parts which suffer from blurring are drawn with a dotted line. The limited view artifacts have been reduced as follows. In the backprojection approach, the image quality has been improved by adding a weighting factor from a smoothing function to the backprojection signals[30]. In the model-based reconstructions, different regularization terms have been used to reduce the artifacts resulting from the limited view scenario[31,32]. Furthermore, it has been shown that utilizing prior structural information can improve the quality of the reconstructed images significantly[33,34]. The Bayesian approach taken in this study offers a natural way to incorporate prior information into the image reconstruction procedure. Therefore, the approach can be utilized in imaging situations with a limited view.

In many image reconstruction algorithms it is assumed that ultrasound detectors are ideal point-like detectors with an infinite bandwidth. The real ultrasound detectors, however, are characterized by finite apertures and finite bandwidths. Both the finite apertures and the finite bandwidths of the detectors can cause blurring of the reconstructed images[35,36]. How-

ever, if the properties of the detectors are taken into account in the model-based inversion, the blurring may be significantly reduced leading to an enhanced image quality[37–39]. In this work, the finite sizes and bandwidths of the acoustic detectors are modeled and included into the solution of the inverse problem.

The rest of the paper is organized as follows. PAT and the Bayesian approach to image reconstruction are described in Sec. II. Then, implementation and results of the numerical simulations are shown in Sec. III. Finally, the results are discussed and conclusions are given in Sec. IV.

II. PHOTOACOUSTIC TOMOGRAPHY

A. Forward problem

In photoacoustic tomography measurement situation, an object is irradiated by a short light pulse. As light propagates within the object, it is absorbed. The energy of the absorbed light causes thermoelastic expansion of the object which in turn leads to localized increases in acoustic pressure. This results in generation of acoustic pressure waves which propagate through the medium and can be measured with detectors on the surface of the object.

Assuming that the object possesses homogeneous acoustic properties and that the duration of the irradiating optical pulse is negligible, the acoustic pressure wavefield satisfies the following homogeneous wave equation

$$\left(\frac{\partial^2}{\partial t^2} - c^2 \nabla^2 \right) p(r, t) = 0 \tag{1}$$

with initial conditions

$$p(r, t = 0) = p_0(r) \tag{2}$$

$$\frac{\partial}{\partial t} p(r, t = 0) = 0, \tag{3}$$

where p is the pressure, r is the spatial position, t is the time, c is the speed of sound and p_0 is the initial pressure distribution, see e.g. Ref. 1 and the references therein.

Since the solution p of (1)-(3) is linear with respect to p_0, it can be written as a matrix-vector multiplication in a discrete case. The discrete observation model for PAT in the presence of additive noise is

$$p_t = K p_0 + e, \tag{4}$$

where $p_t \in \mathbb{R}^m$ is a vector of measured acoustic pressure waves at the detector locations and temporal samples, $p_0 \in \mathbb{R}^n$ is a discrete initial pressure distribution within the object, $K \in \mathbb{R}^{m \times n}$ is the discrete forward model for the pressure propagation which maps the initial pressure distribution to the measurable data, and $e \in \mathbb{R}^m$ denotes the noise. In this work, the matrix K is computed using the k-Wave toolbox[40] using MATLAB (R2011a, The MathWorks Inc., Natick, MA). In practice, the matrix K is assembled by looping over each pixel describing p_0, setting the pixel value to one while keeping the other pixels at zero, computing the acoustic output using k-Wave, and proceeding to the next pixel. The outputs of the k-Wave then form the columns of the matrix K. This corresponds to computing the impulse response of the discrete system approximating (1)-(3).

B. Inverse problem

In photoacoustic tomography, the initial pressure distribution p_0 is reconstructed when the detected pressure signals p_t are given. This is the inverse problem of PAT. In this work, the inverse problem is approached in the framework of the Bayesian inversion[21–23].

Let us assume that p_t and p_0 are random variables in the finite dimensional spaces $\mathbb{R}^m$ and $\mathbb{R}^n$, respectively. The solution of the inverse problem is the posterior probability density $\pi(p_0|p_t)$ which according to Bayes' theorem is

$$\pi(p_0|p_t) = \frac{\pi(p_0)\pi(p_t|p_0)}{\pi(p_t)}, \tag{5}$$

where $\pi(p_0)$ is the prior probability density and $\pi(p_t|p_0)$ is the likelihood density. The prior density represents the prior information of the unknown parameters of interest, whereas the likelihood expresses the likelihood of measurement outcomes with given parameter values. Since $\pi(p_t)$ is constant for a given (fixed) measurement p_t, Eq. (5) can be written in the non-normalized form

$$\pi(p_0|p_t) \propto \pi(p_0)\pi(p_t|p_0). \tag{6}$$

If noise e and parameters p_0 are assumed to be mutually independent, the observation model (4) leads to a likelihood density

$$\pi(p_t|p_0) = \pi_e(p_t - Kp_0), \tag{7}$$

where π_e is the probability distribution of the noise e.

Let the initial pressure distribution p_0 and the measurement noise e be modeled as Gaussian distributions, i.e. $p_0 \sim \mathcal{N}(\eta_{p_0}, \Gamma_{p_0})$ and $e \sim \mathcal{N}(\eta_e, \Gamma_e)$ where $\eta_{p_0} \in \mathbb{R}^n$ and $\Gamma_{p_0} \in \mathbb{R}^{n \times n}$ are the mean and covariance of the prior and $\eta_e \in \mathbb{R}^m$ and $\Gamma_e \in \mathbb{R}^{m \times m}$ are the mean and the covariance of the noise. In this case, the posterior density (6) can be written as

$$\pi(p_0|p_t) \propto \exp\left\{ -\frac{1}{2}\left\|L_e(p_t - Kp_0 - \eta_e)\right\|^2 \right.$$
$$\left. -\frac{1}{2}\left\|L_{p_0}(p_0 - \eta_{p_0})\right\|^2 \right\}, \tag{8}$$

where L_e and L_{p_0} are the Cholesky decompositions of the inverse covariance matrices of the noise and prior, respectively, i.e. $L_e^{\mathrm{T}}L_e = \Gamma_e^{-1}$ and $L_{p_0}^{\mathrm{T}}L_{p_0} = \Gamma_{p_0}^{-1}$. In the case of a linear observation model (4) and Gaussian distributed noise and prior, the posterior density is also a Gaussian distribution

$$p_0|p_t \sim \mathcal{N}(\eta_{p_0|p_t}, \Gamma_{p_0|p_t}), \tag{9}$$

where

$$\eta_{p_0|p_t} = A^{-1}b, \tag{10}$$
$$\Gamma_{p_0|p_t} = A^{-1}, \tag{11}$$

are the mean and covariance, respectively, where

$$A = K^{\mathrm{T}}\Gamma_e^{-1}K + \Gamma_{p_0}^{-1}$$
$$b = K^{\mathrm{T}}\Gamma_e^{-1}(p_t - \eta_e) + \Gamma_{p_0}^{-1}\eta_{p_0}.$$

The practical solution for the inverse problem is obtained by calculating point estimates of the posterior density. In this work, we consider the MAP estimate with its credible intervals. The MAP estimate of (8) is obtained by minimizing the negative of the exponent term, that is

$$p_{0,\text{MAP}} = \arg\min_{p_0} \ \|L_e(p_t - Kp_0 - \eta_e)\|^2$$
$$+ \|L_{p_0}(p_0 - \eta_{p_0})\|^2 . \tag{12}$$

In the purely Gaussian case considered here, the MAP estimate is the mean of the posterior distribution $p_{0,\text{MAP}} = \eta_{p_0|p_t}$ given in Eq. (10). As it can be seen, the MAP estimate resembles the solution of a minimization problem of a generalized Tikhonov regularization. In fact, the Tikhonov regularization can be derived using a Bayesian approach by making some specific assumptions of the distribution of the noise and prior.

The credible interval of the estimated parameter p_0 is determined by considering the marginal density of the posterior distribution. The marginal density of the kth element of p_0 is defined as

$$p_{0,k}|p_t \sim \mathcal{N}(\eta_{p_0|p_t,k}, \Gamma_{p_0|p_t,kk}), \tag{13}$$

where $\eta_{p_0|p_t,k}$ is the kth element of $\eta_{p_0|p_t}$ and $\Gamma_{p_0|p_t,kk}$ is the kth diagonal element of $\Gamma_{p_0|p_t}$. Now, for example, a 99.7 % credible interval of the $p_{0,k}$ is

$$\left[\eta_{p_0|p_t,k} - 3\sqrt{\Gamma_{p_0|p_t,kk}} \ , \ \eta_{p_0|p_t,k} + 3\sqrt{\Gamma_{p_0|p_t,kk}}\right] . \tag{14}$$

1. Prior model

The prior density expresses what is known about the unknown parameter of interest prior to the experiment. In this work, two prior models, a white noise prior and a Matérn prior[41], are utilized. Both of them are Gaussian priors, that is, they can be described by their means η_{p_0} and covariance matrices Γ_{p_0}. The mean and variance of the prior are chosen based on prior knowledge on the unknown parameters of interest. In many practical applications, the range of the unknown parameter values is roughly known and this information is then utilized.

In the case of the white noise prior, the covariance matrix is a diagonal matrix with the values of variance σ_w^2 on the diagonal

$$\Gamma_{p_0} = \text{diag}(\sigma_{\text{w}}^2). \tag{15}$$

The white noise prior is well suited for the estimation of parameters which are independent of each other or which have no spatial correlation. In tomography, this relates to a non-smooth spatial distribution of the estimated parameters. Although the white noise prior can not be regarded as the most suitable prior model for PAT, where some spatial correlation in parameter values between the pixels can be expected, it is commonly used in Tikhonov regularization, and therefore it is also chosen for consideration in this work.

The Matérn prior, on the other hand, supports correlation between pixels. It promotes distributions which can be locally close to homogeneous with sharp changes between different areas. An example of such distribution could be blood vessels in photoacoustic imaging. In
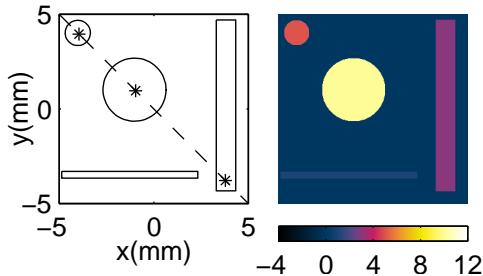
FIG. 2. (Color online) A graph of the simulation domain (left) and the true initial pressure distribution (right). The asterisks indicate the locations where the marginal densities are plotted and the dashed line indicates the location where the credible interval is plotted.

the case of the Matérn prior, the covariance matrix is defined by the Matérn covariance function[41]

$$\Gamma_{p_0,ij} = \sigma_m^2 \frac{2^{1-\nu}}{G(\nu)} \left(\frac{\sqrt{2\nu} \|r_i - r_j\|}{l} \right)^\nu$$
$$\cdot K_\nu \left(\frac{\sqrt{2\nu} \|r_i - r_j\|}{l} \right), \qquad (16)$$

where i and j are the element indices, r_i and r_j are the corresponding pixel locations, σ_m^2 is the variance, $\nu > 0$ is the smoothness parameter, l is the characteristic length scale, G is the gamma-function, and K_ν is the modified Bessel function of the second kind of order ν. The smoothness parameter ν controls the smoothness of the random field, while the characteristic length scale l controls the spatial range of correlation. In practice, some prior information about the structures and their size inside the target medium are known, and thus the correlation range can be chosen based on that knowledge.

III.   NUMERICAL SIMULATIONS

The Bayesian approach to the PAT inverse problem was tested with simulations. Three problems were considered. First, the effect of the detector geometry and the prior model on image reconstruction was investigated. In that study, idealized point-like detectors were used. In the second problem, the detectors were considered to have a finite aperture and in the third study, detectors with limited bandwidth were investigated.

In all simulations, a two dimensional square domain of size $10\,\mathrm{mm} \times 10\,\mathrm{mm}$ was considered. A graph of the simulation domain and the initial pressure distribution are shown in Fig. 2. The domain contained four different inclusions: two different size circles and two different size rectangles. The domain was assumed to be a homogeneous with the speed of sound $c = 1500\,\mathrm{m/s}$. Acoustic attenuation was not considered.

Four types of detector geometries were considered: a four sided (4-side), a two-sided L-shaped (L-shape), a one-sided (1-side), and a one-sided plus three detectors (1-side+3).

8

In the 4-side detector geometry, the detectors were evenly positioned on the boundary surrounding the whole domain. In the L-shape detector geometry, the detectors were located on two adjacent sides of the domain. The detectors were located on sides $y = 5\,\mathrm{mm}$ and $x = -5\,\mathrm{mm}$. In the 1-side detector geometry, the detectors were positioned only on one side ($y = 5\,\mathrm{mm}$) of the domain. The 1-side+3 detector geometry was similar to the 1-side detector geometry but it also included additional detectors at the center of the other edges. The detector geometries are shown in Fig. 3.

A. Data simulation

Data was simulated using an initial pressure distribution shown on the right image of Fig. 2 with the k-space time-domain method implemented with the k-Wave MATLAB toolbox. For data simulation, the $10\,\mathrm{mm} \times 10\,\mathrm{mm}$ target domain was discretized into 300×300 pixels (pixel width $\Delta h = 33.33\,\mu\mathrm{m}$). For the numerical implementation with the k-Wave, this discretization was increased on the boundary of the domain with a layer of thickness $2.5\,\mathrm{mm}$ (75 pixels). This layer was used to place the acoustic detectors outside the target. The discretization was further extended with a perfectly matched layer (PML) with thickness of $2\,\mathrm{mm}$ (60 pixels) to avoid boundary reflections (numerical artifacts). Thus, the size of the complete discretized simulation domain of k-Wave was 570×570 pixels with pixel width $\Delta h = 33.33\,\mu\mathrm{m}$. The pressure signals were recorded at detector locations using 283 temporal samples from $0\,\mu\mathrm{s}$ to $14.1\,\mu\mathrm{s}$ with $50\,\mathrm{ns}$ time step (sampling frequency $20\,\mathrm{MHz}$). This corresponds to an acoustic propagation distance of $21.15\,\mathrm{mm}$. Uncorrelated Gaussian distributed noise with a zero mean $\eta_e = 0$ and a standard deviation σ_e proportional to the peak amplitude of the simulated pressure signal was added to the signal. The noise levels investigated were $1\,\%$ and $5\,\%$ of the peak positive amplitude. In the case of the detectors with a limited bandwidth, the simulated signal was bandpass filtered first and then noise was added to the filtered data.

B. Inverse problem

In the inverse problem, the $10\,\mathrm{mm} \times 10\,\mathrm{mm}$ target domain was discretized using 120×120 pixels ($\Delta h = 83.33\,\mu\mathrm{m}$). For the numerical implementation, the discretization was extended with a layer of thickness $2.5\,\mathrm{mm}$ (30 pixels) containing the acoustic detectors and a PML of thickness $2\,\mathrm{mm}$ (24 pixels). The matrix K was formed as described in Sec. II A by computing the model output for the pixels located inside the target domain.

   Two prior densities described in Sec. II B 1 were used: the white noise prior and the Matérn prior. For both priors, the mean was set as the expected mean value of the initial pressure $\eta_{p_0} = 5$ and the variance was set as $\sigma_w = \sigma_m = 2.5$ which means that $99.7\,\%$ of initial pressure values were expected to be normally distributed within range $[-2.5\,, 12.5]$. For the Matérn prior, the characteristic length scale of $l = 1.25\,\mathrm{mm}$ and the smoothness parameter of $\nu = 0.5$ were used. The measurement noise was considered to be uncorrelated Gaussian distributed noise with zero mean and standard deviation σ_e, that is $\eta_e = 0$ and $L_e = \mathrm{diag}(1/\sigma_e)$. The standard deviation was set as $1\,\%$ or $5\,\%$ of the peak positive amplitude of the noisy simulated data.

TABLE I. The number of the detectors used in the simulations in the 4-side, L-shape, 1-side and 1-side+3 detector geometries using ideal detectors (ideal), finite size detectors (finite), and detectors with a limited bandwidth (BPF).

	Ideal	Finite	BPF
4-side	164	20	164
L-shape	83	10	83
1-side	42	5	42
1-side+3	45	8	45

The MAP estimates of the initial pressure distribution $p_{0,\mathrm{MAP}}$ were computed using Eq. (10). The difference between the simulated and the estimated initial pressure distribution was compared by computing the relative error

$$E_{p_0} = 100\% \cdot \frac{\|p_0 - \hat{p}_0\|}{\|p_0\|}, \tag{17}$$

where p_0 is the simulated initial pressure distribution and $\hat{p}_0$ is the estimated value interpolated to the simulation grid. The marginal densities were calculated in three locations inside the domain using Eq. (13). These locations are indicated with asterisks in the left image of Fig. 2. Furthermore, the 99.7 % credible intervals were computed on a diagonal cross-section (dashed line in the left image of Fig. 2) using Eq. (14).

C. Detector geometry

First, the effect of the detector geometry and the prior model on the solution of the inverse problem was investigated. The detectors were modeled as ideal point-like detectors with a bandwidth only limited by the temporal sampling. The number of the detectors in each measurement geometry is given in Table I and the locations of the detectors are indicated with dots in Fig. 3. Two noise levels: 1 % and 5 % were considered.

The MAP estimates of the initial pressure distribution obtained using different detector geometries are shown in Figs. 3 and 4 for 1 % and 5 % noise level, respectively. As it can be seen, the estimates obtained using the 4-side and L-shape detector geometries look qualitatively very similar to the true initial pressure distribution with both noise levels. However, some stripe artifacts can be seen in the area which is not enclosed by the detectors in the case of the L-shape detector geometry. These stripe artifacts are also visible in the estimates obtained using the 1-side and 1-side+3 detector geometries. Similar stripe artifacts were also observed in Ref. 31. Overall, the quality of the images obtained using the 1-side detector geometry is significantly worse than in the case of the 4-side and L-shape detector geometries. In the 1-side case, the larger circular inclusion is partially distorted and only the top of the larger rectangular inclusion is visible. On the other hand, the quality of the estimates can evidently be improved if one extra detector is added to each 'empty' side

TABLE II. The relative errors of the MAP estimates (in percentage) calculated in the 4-side, L-shape, 1-side and 1-side+3 detector geometries using the ideal detectors (ideal), finite size narrow (finite-N) and wide (finite-W) detectors, and detectors with limited bandwidths (BPF-3 and BPF-6). In the case of the ideal detectors, both white noise and Matérn priors, and noise levels 1 % and 5 % were used.

	Ideal(white noise)		Ideal(Matérn)		Finite-W	Finite-N	BPF-3	BPF-6
	1%	5%	1%	5%				
4-side	13.2	18.2	12.6	15.1	24.3	23.0	12.6	14.0
L-shape	15.9	22.7	14.9	17.3	30.2	32.6	15.4	19.2
1-side	35.9	54.1	34.0	39.3	53.4	56.0	36.7	50.6
1-side+3	26.1	43.9	27.4	28.7	34.7	34.9	30.1	33.2

(the 1-side+3 detector geometry). This can be seen on the bottom row of Figs. 3 and 4. The estimates obtained using the 4-side, L-shape, 1-side, and 1-side+3 detector geometries correspond to the theory and the results described in Ref. 29. Differences between the estimates obtained using the different prior models are almost indistinguishable in the case of the 4-side and L-shape detector geometries. However, in the case of the 1-side and 1-side+3 detector geometries, the reconstructed images obtained using the Matérn prior have better quality than the images obtained using the white noise prior. This is especially evident if the noise level is higher. This indicates that, as the inverse problem becomes more ill-posed, the relevance of a good prior information increases.

The relative errors of the estimates are given in Table II. As it can be seen, the relative errors of the estimates obtained using the 4-side detector geometry have the smallest values. The errors increase as the number of detection edges decrease. With the 1 % noise level, the relative errors of the estimates obtained using the Matérn prior are slightly smaller than relative errors of the estimates obtained using the white noise prior in all detector geometries apart from the 1-side+3 detector geometry. On the other hand, with 5% noise level, the relative errors of the estimates obtained using the white noise prior are significantly larger than the relative errors of the estimates obtained using Matérn prior in all detector geometries. This is especially evident in the 1-side and 1-side+3 detector geometries.

The marginal densities in the three locations of the domain indicated in Fig. 2 are shown in Figs. 5 and 6 for the noise levels 1 % and 5 %, respectively. The marginal densities are shown for the 4-sided, L-shaped, and 1-side detector geometries and for the both prior distributions. As it can be seen, the marginal densities in the case of 4-side detector geometry are narrower than in the cases of L-shape and 1-side detector geometries. It can also be seen that, in the case of L-shape detector geometry, the marginal densities in the point located outside the region enclosed by the detectors are significantly wider than in the points located inside the region enclosed by the detectors. The results indicate that the uncertainties of the estimates obtained using the 4-side detector geometry are smaller than the uncertainties of the estimates obtained using the L-shape and 1-side geometries. This is valid also in those locations of the L-shape geometry which are enclosed by the detectors. The figures also
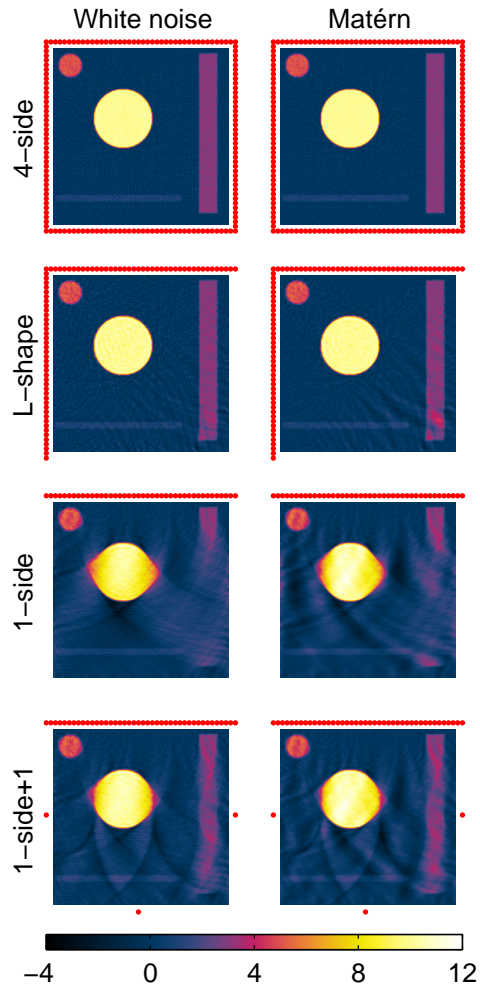
FIG. 3. (Color online) The MAP estimates obtained using the white noise prior (first column) and the Matérn prior (second column) in the case of the ideal detectors. The noise level was 1 %. From top to bottom: 4-side (first row), L-shape (second row), 1-side (third row) and 1-side+3 (fourth row) detector geometries. The dots indicate the locations of the detectors.
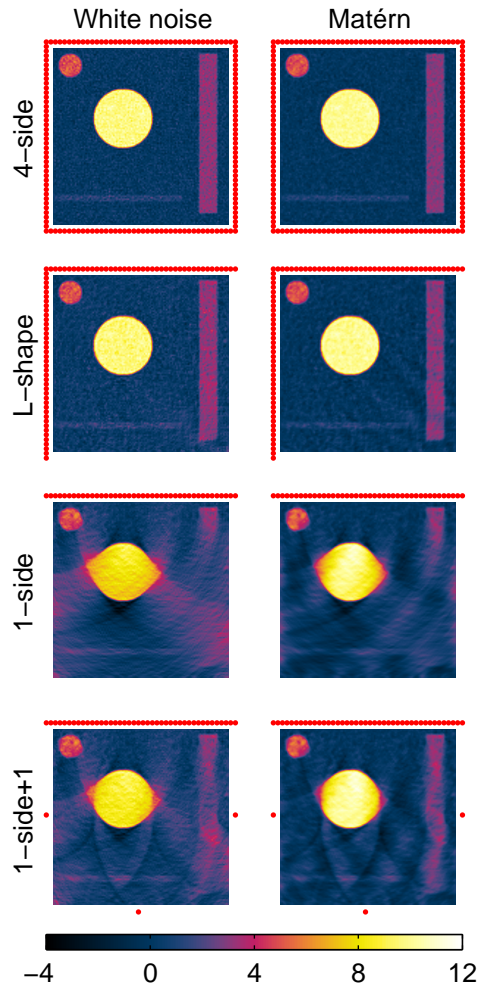
FIG. 4. (Color online) The MAP estimates obtained using the white noise prior (first column) and the Matérn prior (second column) in the case of the ideal detectors. The noise level was 5 %. From top to bottom: 4-side (first row), L-shape (second row), 1-side (third row) and 1-side+3 (fourth row) detector geometries. The dots indicate the locations of the detectors.

13

show that the maximum of the marginal distribution is not necessarily at the location of the true value. However, the true value is within the principal support of the distribution in each case. This indicates that the error estimates are reliable. Comparing different prior distributions and noise levels support the results that the Matérn prior and lower noise levels produce more accurate estimates.

The MAP estimates together with 99.7 % credible intervals on a diagonal cross-section through the domain in the case of 1 % noise level are shown in the Fig. 7. As it can be seen, the credible intervals in the case of the 4-side detector geometry are narrow which indicates the accuracy of the MAP estimate. In the case of the L-shape, 1-side, and 1-side+3 detector geometries, the credible intervals are wide which can especially be seen in the areas which are not enclosed by the detectors. It can also be seen that the credible intervals in the case of the 1-side+3 detector geometry are narrower than in the case of the 1-side detector geometry which indicates that the uncertainty of the estimates in the 1-side+3 case is smaller than in the 1-side case. Furthermore, the credible intervals are narrower when the Matérn prior is used.

Since better estimates were obtained using the Matérn prior than with the white noise prior, the Matérn prior was chosen to be used in the following simulations. Furthermore, only the noise level of 1 % was considered.

D.   Finite size detectors

In the second study, the acoustic detectors were modeled as finite size, which is a more realistic approach than the idealized detectors considered in the first study. Two different widths of the detectors were considered: narrow detectors of the width 0.5 mm and wide detectors of the width 1.5 mm. Both detector setups had the pitch (element center to element center spacing) of 2 mm. The number of the detectors in different detector geometries is given in Table I. The locations of the detectors are indicated in Fig. 8 with lines.

The MAP estimates of the initial pressure distribution are shown in Fig. 8. The main features in the reconstructed images obtained using the finite size detectors are similar to the images obtained using the ideal detectors. However, the background and the rectangular inclusions are not as uniform as in the case of the ideal detectors. The wider detectors cause blurring of the estimates due to the narrower directivity pattern of the detecting element, and therefore quality of the estimates is not as good as with the ideal detectors.

The relative errors of the estimates are given in Table II. The relative errors obtained using the finite size detectors are larger than in the case of the ideal detectors. Furthermore, the relative errors obtained using the wide and narrow detectors are approximately the same. That is, although the wider detectors cover almost the entire surface area, they do not produce better estimates than the same number of narrow detectors.

The MAP estimates together with the 99.7 % credible intervals on a diagonal cross-section through the domain obtained using the finite size detectors in the different detector geometries are shown in Fig. 9. As it can be seen, the credible intervals are narrower in the case of 4-side detector geometry than in the case of other detector geometries. Also, the L-shape detector geometry gives narrower distribution than the 1-side geometry. Compared with the results of the ideal point-like detectors, the finite size detectors give wider credible intervals in the regions which are enclosed by detectors. This is due to the fact that there
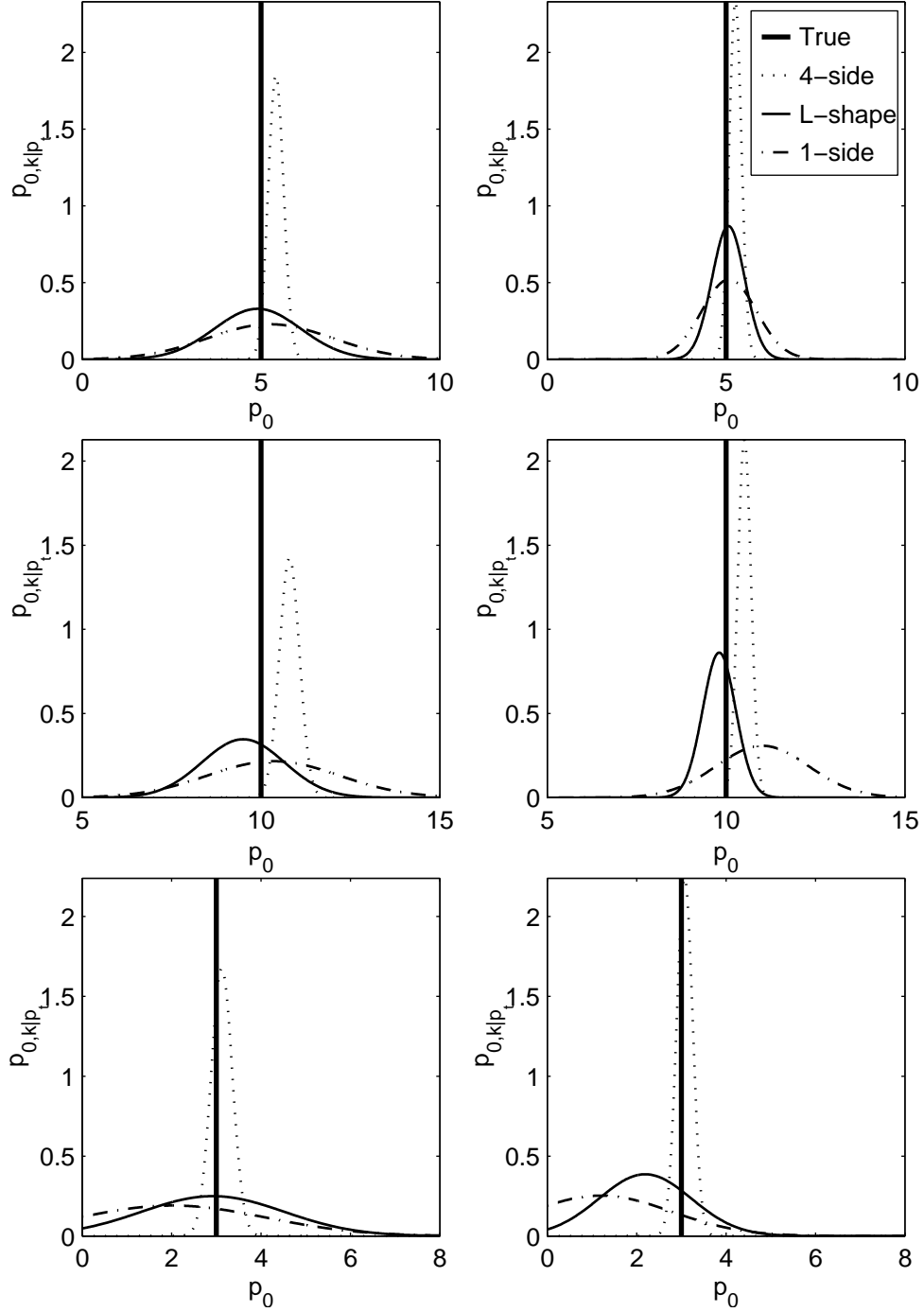
14

FIG. 5. The marginal densities in three different locations of the domain obtained using the white noise prior (first column) and the Matérn prior (second column) in different detector geometries in the case of the ideal detectors. The noise level was 1 %. The locations where the marginal densities are plotted are indicated in Fig. 2 with asterisks and are positioned from top to bottom order respectively.
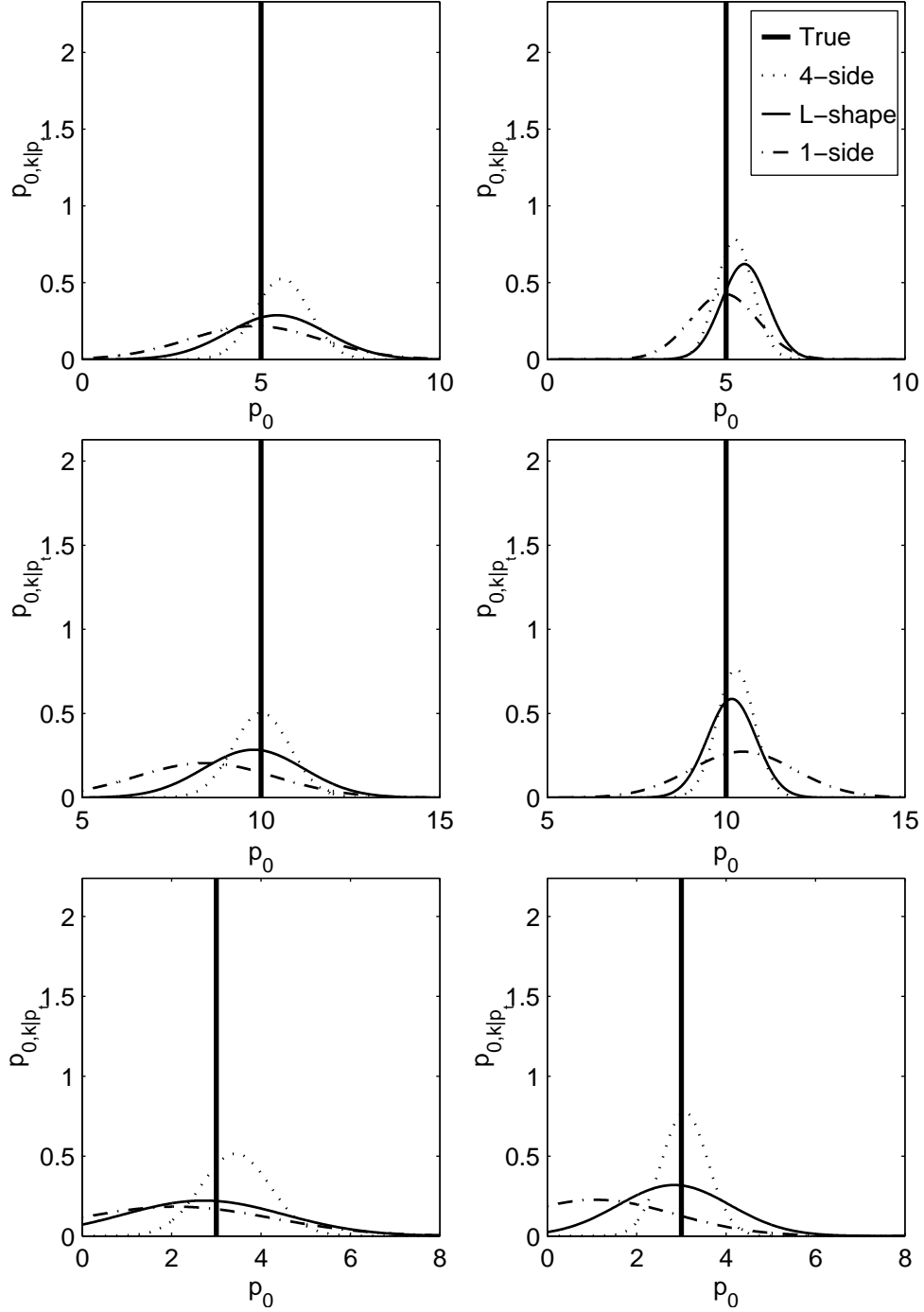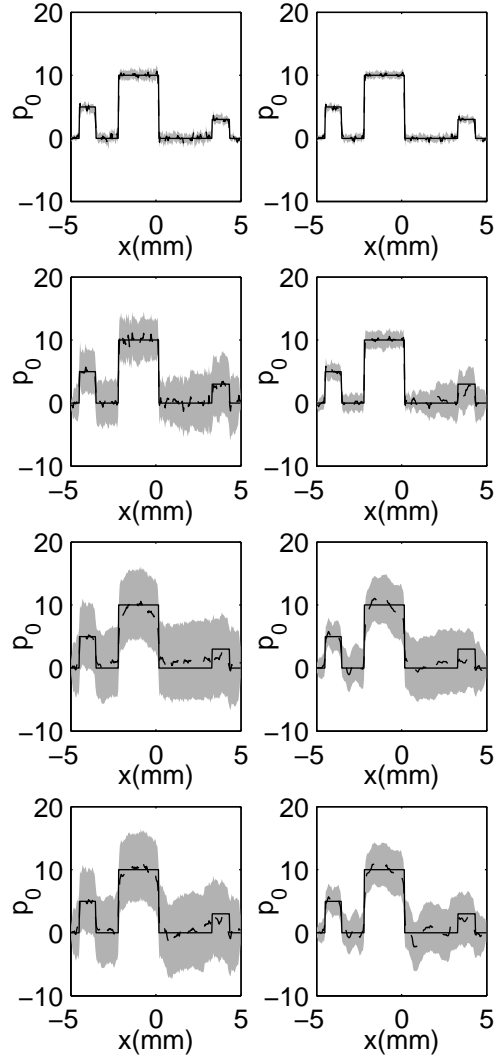
FIG. 6. The marginal densities in three different locations of the domain obtained using the white noise prior (first column) and the Matérn prior (second column) in different detector geometries in the case of the ideal detectors. The noise level was 5 %. The locations where the marginal densities are plotted are indicated in Fig. 2 with asterisks and are positioned from top to bottom order respectively.

FIG. 7. The true initial pressure distribution (solid line) and the MAP estimate (dashed line) with the 99.7 % credible interval (gray area) on a diagonal cross-section through the domain obtained using the white noise prior (first column) and the Matérn prior (second column) in the case of the ideal detectors. The noise level was 1 %. From top to bottom: 4-side (first row), L-shape (second row), 1-side (third row) and 1-side+3 (fourth row) detector geometries.
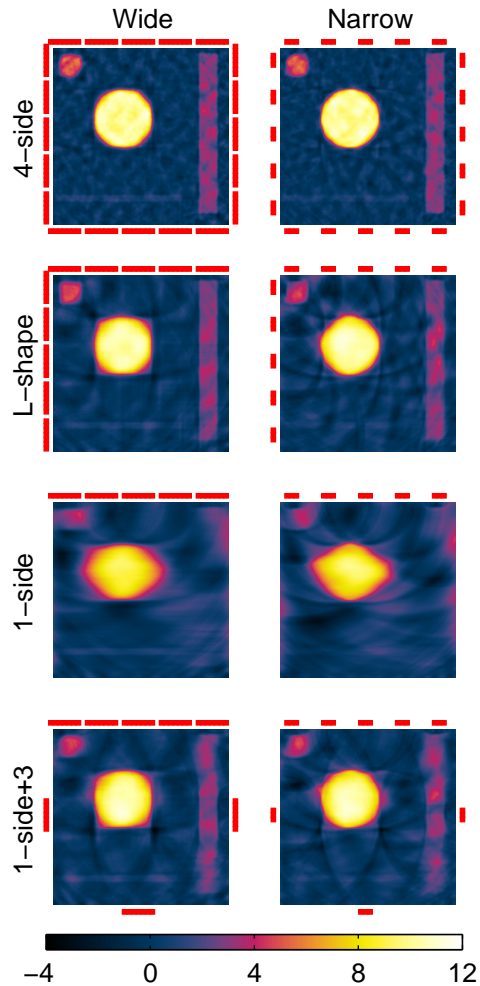
FIG. 8. (Color online) The MAP estimates obtained using wide (first column) and narrow (second column) finite size detectors in different detector geometries. From top to bottom: 4-side (first row), L-shape (second row), 1-side (third row) and 1-side+3 (fourth row) detector geometries. The Matérn prior was used. The noise level was 1 %. The lines indicate the locations of the detectors.

are less detectors and due to the averaging effect of the finite size detectors.

E.   Finite bandwidth

In the third study, the detectors were modeled as point-like detectors with a finite bandwidth. The frequency response of the band-limited detectors was modeled as a bandpass filter with -6 dB bandwidth of roughly 8 MHz. Two different central frequencies were considered: 3 MHz (BPF-3) and 6 MHz (BPF-6). The bandpass filter was generated using MATLAB's `butter` function. The number of the detectors in different detector geometries was the same as in the case of the ideal detectors and it is given in Table I. The locations of the detectors are shown in Fig. 10 with dots.

The MAP estimates of the initial pressure distribution are shown in Fig. 10. As it can be seen, the estimates obtained using the lower bandwidth (BPF-3) are similar to the estimates obtained using the ideal detectors. In the case of the upper bandwidth (BPF-6), the estimates resemble the estimates obtained using the BPF-3 and the ideal detectors, however, some of the artifacts are more visible.

The relative errors of the estimates are given in Table II. As it can be seen, the relative errors of the estimates obtained using the lower bandwidth (BPF-3) are approximately of the same magnitude as the relative errors of estimates obtained using the ideal detectors in the cases of 4-side and L-shape measurement geometries. However, when the number of detecting sides decreases, the errors of the estimates obtained using lower bandwidth (BPF-3) increase. It can also be seen that the relative errors obtained using the upper bandwidth (BPF-6) are larger than the relative errors obtained using BPF-3 and ideal detectors.

The MAP estimates together with the 99.7 % credible intervals on a diagonal cross-section through the domain obtained using the band-limited detectors in different detector geometries are shown in Fig. 11. The credible intervals obtained using the lower bandwidth (BPF-3) are narrower or approximately the same as the credible intervals obtained using the upper bandwidth (BPF-6). Compared to the ideal detectors, the credible intervals are wider or approximately the same for the both band-limited detectors.

The better reconstructions obtained with the lower central frequency filter BPF-3 are due to the fact that the simulated data (corresponding to p_0 in Fig 2) contains more information in the frequency range of the BPF-3 than in the range of BPF-6. This can be verified for example by computing the norm of the difference between the ideal and filtered data and comparing the results between them. Thus, in the case of p_0 considered in the simulations, higher central frequency bandpass filter results in lower quality data which leads into lower quality estimates.

IV.   DISCUSSION AND CONCLUSIONS

In this work, the Bayesian approach to PAT image reconstruction with uncertainty quantification was described. In the Bayesian approach, all parameters are treated as random variables and the solution of the inverse problem, the posterior density, is obtained based on the knowledge of the measurements, the model, and the prior information. Different point estimates can be calculated from the posterior density. In this work, the MAP estimate with
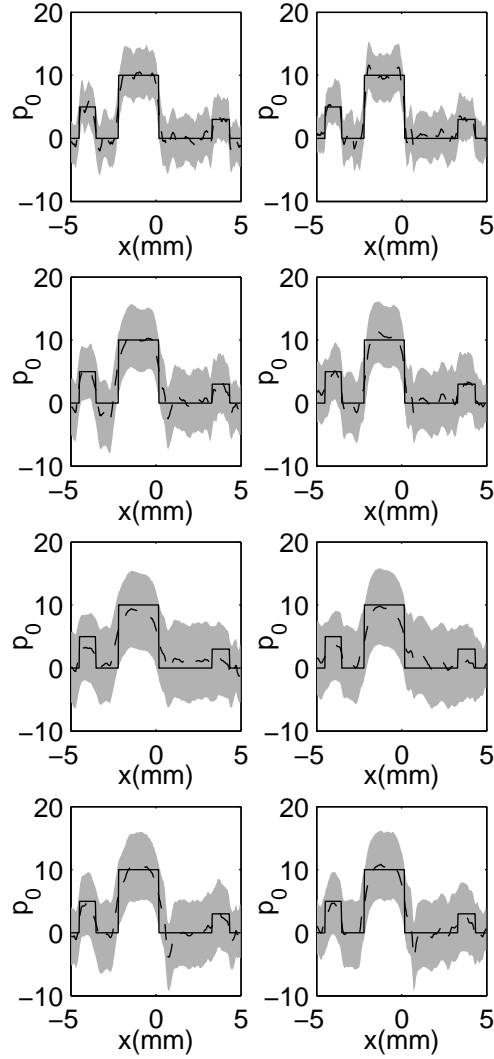
FIG. 9. The true initial pressure distribution (solid line) and the MAP estimate (dashed line) with the 99.7 % credible interval (gray area) on a diagonal cross-section through the domain obtained using the wide (first column) and the narrow (second column) finite size detectors. From top to bottom: 4-side (first row), L-shape (second row), 1-side (third row) and 1-side+3 (fourth row) detector geometries. The Matérn prior was used. The noise level was 1 %.
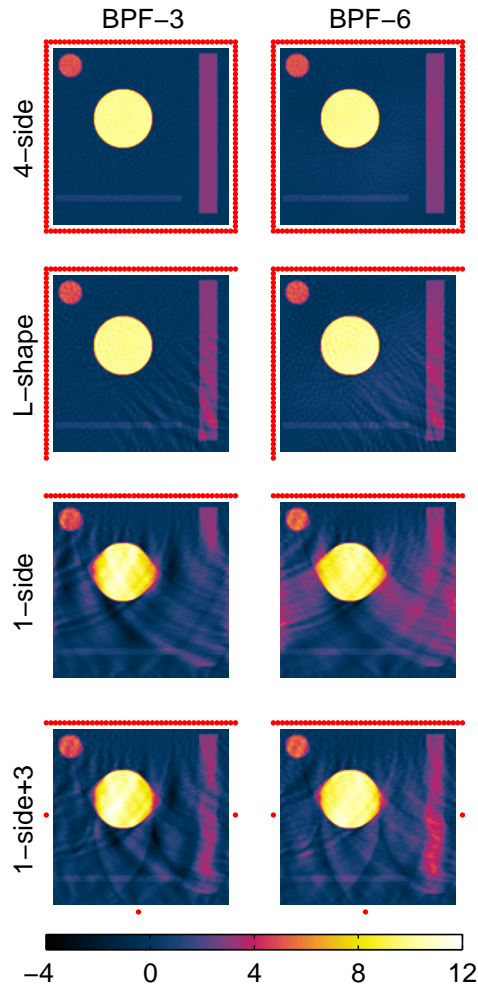
FIG. 10. (Color online) The MAP estimates obtained using the BPF-3 (first column) and the BPF-6 (second column) band-limited detectors in different detector geometries. From top to bottom: 4-side (first row), L-shape (second row), 1-side (third row) and 1-side+3 (fourth row) detector geometries. The Matérn prior was used. The noise level was 1 %. The dots indicate the locations of the detectors.
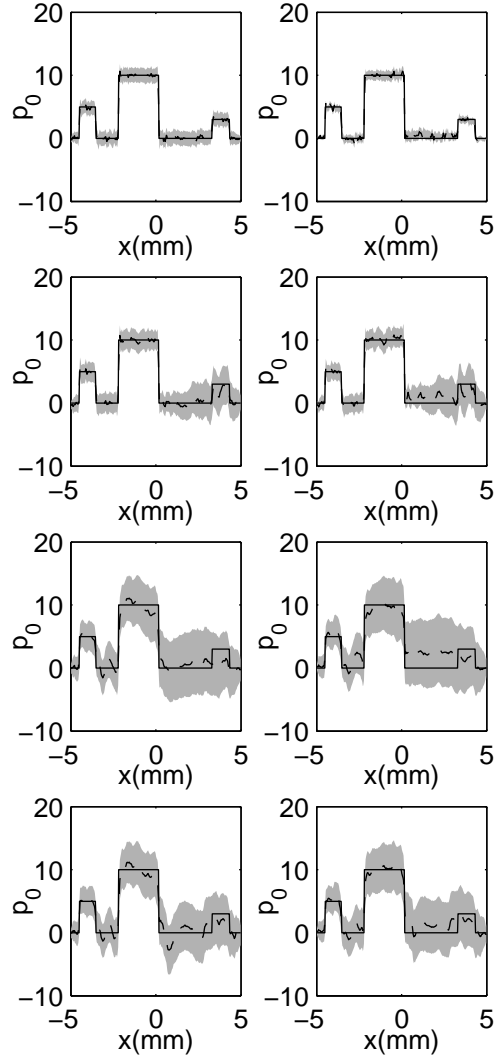
FIG. 11. The true initial pressure distribution (solid line) and the MAP estimate (dashed line) with the 99.7 % credible interval (gray area) on a diagonal cross-section through the domain obtained using the BPF-3 (first column) and the BPF-6 (second column) band-limited detectors. From top to bottom: 4-side (first row), L-shape (second row), 1-side (third row) and 1-side+3 (fourth row) detector geometries. The Matérn prior was used. The noise level was 1 %.

22

credible intervals was considered. The credible intervals give information of the uncertainty of the reconstructed image. Such information can be useful in interpretation how reliable the reconstructed images are. Furthermore, it could be an aid, for example, in the design of the PAT measurement setup.

The Bayesian approach was investigated using simulated PAT data. MAP estimates were computed from simulated data in various imaging situations. The relative errors between the simulated and the estimated initial pressure distributions were computed to compare the estimates quantitatively. In addition, the marginal density distributions and the 99.7 % credible intervals were determined.

The Bayesian approach enables a natural way to include prior information of the estimated parameters into the reconstruction. In this work, the white noise and the Matérn priors were used. It was observed that the Matérn prior produced better estimates. This is due to the fact that the Matérn prior supports estimates with a spatial correlation whereas white noise prior assumes all the estimated parameters to be uncorrelated. In the future, utilizing other prior distributions will be investigated. For example, the total variation prior and including structural prior information have been found to provide good photoacoustic images[32,33]. Furthermore, other prior models such as anatomical, and sample based priors, that are determined by the tissue optical properties coupled with the model for light propagation and absorption, could be developed.

In this work, both full view and different limited view detector geometries were investigated. It was shown that the Bayesian approach can be used to provide photoacoustic images also in limited view imaging situations. The estimates obtained using a full view scenario were accurate and the uncertainties of these estimates were small. However, in the limited view reconstructions, artifacts were visible and the uncertainties of the estimates were larger. Different type of detectors were investigated. The finite size of detectors provided poorer quality MAP estimates with larger uncertainties when compared to the results obtained using the ideal point-like detectors. Also the band-limited frequency response decreased the quality of the estimates when compared to the ideal detectors. In all cases, the uncertainty estimates given by the approach were reliable, which indicates that the Bayesian approach can provide reliable error limits.

In this work, the proposed approach was tested in a simple two dimensional geometry. In the future, three dimensional situation and more realistic tissue-like structures will be considered. Furthermore, in this work, the whole system matrix was formed by simulating the system response of each pixel. Although, the approach can be implemented in two dimensions, it would be a computationally too expensive approach in three dimensions. Therefore, an alternative approach to the solution of the inverse problem will be developed when the method will be extended to three dimensions.

A common assumption in the PAT reconstruction algorithms, also assumed in this work, is the non-attenuating and homogeneous medium with a constant speed of sound. However, several tissue types have acoustic impedance variations, and thus the reconstructed images can contain significant distortions and artifacts if the inhomogeneous acoustic properties of the object are not taken into account in the reconstruction algorithm. Therefore, several PAT algorithms which aim to improve the image quality by taking into account the inhomogeneous acoustic properties of object have been developed e.g. in Refs. 14,42–46. In the future, the Bayesian approach could be utilized in compensating the errors caused by the uncertainties

in the acoustic parameters.

Estimation of the initial pressure distribution in PAT does not differ significantly from the estimation of the initial pressure distribution in thermoacoustic tomography (TAT), where the excitation is performed using microwave radiation. For this reason, the findings of this study are applicable to TAT as well and the Bayesian approach presented can be applied with relatively small modifications.

Acknowledgements

REFERENCES

1. C. Li and L. V. Wang, "Photoacoustic tomography and sensing in biomedicine," Phys. Med. Biol., **54**(19), R59–R97 (2009).

2. P. Beard, "Biomedical photoacoustic imaging," Interface Focus, **1**(4), 602–631 (2011).

3. M. Xu and L. V. Wang, "Photoacoustic imaging in biomedicine," Rev. Sci. Instrum., **77**(4), 041101(22pp) (2006).

4. C. Lutzweiler and D. Razansky, "Optoacoustic imaging and tomography: Reconstruction approaches and outstanding challenges in image performance and quantification," Sensors (Switzerland), **13**(6), 7345–7384 (2013).

5. A. Rosenthal, V. Ntziachristos, and D. Razansky, "Acoustic inversion in optoacoustic tomography: A review," Curr. Med. Imaging Rev., **9**(4), 318–336 (2013).

6. L. A. Kunyansky, "A series solution and a fast algorithm for the inversion of the spherical mean Radon transform," Inverse Probl., **23**(6), S11–S20 (2007).

7. M. Agranovsky and P. Kuchment, "Uniqueness of reconstruction and an inversion procedure for thermoacoustic and photoacoustic tomography with variable sound speed," Inverse Probl., **23**(5), 2089–2102 (2007).

8. M. Xu, Y. Xu, and L. V. Wang, "Time-domain reconstruction algorithms and numerical simulations for thermoacoustic tomography in various geometries," IEEE Trans. Biomed. Eng., **50**(9), 1086–1099 (2003).

9. M. Xu and L. V. Wang, "Universal back-projection algorithm for photoacoustic computed tomography," Phys. Rev. E Stat. Nonlin. Soft Matter Phys., **71**(1), 016706(7pp) (2005).

10. L. A. Kunyansky, "Explicit inversion formulae for the spherical mean Radon transform," Inverse Probl., **23**(1), 373–383 (2007).

11. D. Finch, S. K. Patch, and Rakesh, "Determining a function from its mean values over a family of spheres," SIAM J. Math. Anal., **35**(5), 1213–1240 (2004).

12. Y. Xu and L. V. Wang, "Time reversal and its application to tomography with diffracting sources," Phys. Rev. Lett., **92**(3), 339021–339024 (2004).

13. P. Burgholzer, G. J. Matt, M. Haltmeier, and G. Paltauf, "Exact and approximative imaging methods for photoacoustic tomography using an arbitrary detection surface," Phys. Rev. E Stat. Nonlin. Soft Matter Phys., **75**(4), 046706(10pp) (2007).

14. Y. Hristova, P. Kuchment, and L. Nguyen, "Reconstruction and time reversal in thermoacoustic tomography in acoustically homogeneous and inhomogeneous media," Inverse Probl., **24**(5), 055006(25pp) (2008).

15. X. L. Den-Ben, A. Buehler, V. Ntziachristos, and D. Razansky, "Accurate model-based reconstruction algorithm for three-dimensional optoacoustic tomography," IEEE Trans. Med. Imag., **31**(10), 1922–1928 (2012).

16. A. Rosenthal, D. Razansky, and V. Ntziachristos, "Fast semi-analytical model-based acoustic inversion for quantitative optoacoustic tomography," IEEE Trans. Med. Imag., **29**(6), 1275–1285 (2010).

17. X. L. Den-Ben, V. Ntziachristos, and D. Razansky, "Acceleration of optoacoustic model-based reconstruction using angular image discretization," IEEE Trans. Med. Imag., **31**(5), 1154–1162 (2012).

18. J. Zhang, M. A. Anastasio, P. J. L. Rivire, and L. V. Wang, "Effects of different imaging models on least-squares image reconstruction accuracy in photoacoustic tomography," IEEE Trans. Med. Imag., **28**(11), 1781–1790 (2009).

19. G. Paltauf, J. A. Viator, S. A. Prahl, and S. L. Jacques, "Iterative reconstruction algorithm for optoacoustic imaging," J. Acoust. Soc. Am., **112**(4), 1536–1544 (2002).

20. K. Wang, R. Su, A. A. Oraevsky, and M. A. Anastasio, "Investigation of iterative image reconstruction in three-dimensional optoacoustic tomography," Phys. Med. Biol., **57**(17), 5399–5423 (2012).

21. J. Kaipio and E. Somersalo, *Statistical and Computational Inverse Problems.* (Springer Science & Business Media, New York, NY, 2006).

22. A. Tarantola, *Inverse Problem Theory and Methods for Model Parameter Estimation.* (Society for Industrial and Applied Mathematics, Philadelphia, 2005).

23. D. Calvetti and E. Somersalo, *An Introduction to Bayesian Scientific Computing: Ten Lectures on Subjective Computing.* (Springer Science & Business Media, New York, NY, 2007).

24. T. Tarvainen, A. Pulkkinen, B. T. Cox, J. P. Kaipio, and S. R. Arridge, "Bayesian image reconstruction in quantitative photoacoustic tomography," IEEE Trans. Med. Imag., **32**(12), 2287–2298 (2013).

25. A. Pulkkinen, B. T. Cox, S. R. Arridge, J. P. Kaipio, and T. Tarvainen, "A Bayesian approach to spectral quantitative photoacoustic tomography," Inverse Probl., **30**(6), 065012(18pp) (2014).

26. S. R. Arridge, J. P. Kaipio, V. Kolehmainen, M. Schweiger, E. Somersalo, T. Tarvainen, and M. Vauhkonen, "Approximation errors and model reduction with an application in optical diffusion tomography," Inverse Probl., **22**(1), 175–195 (2006).

27. V. Kolehmainen, T. Tarvainen, S. R. Arridge, and J. P. Kaipio, "Marginalization of uninteresting distributed parameters in inverse problemsapplication to diffuse optical tomography," Int. J. Uncertain. Quantif., **1**(1), 1–17 (2011).

28. J. Koponen, T. Huttunen, T. Tarvainen, and J. Kaipio, "Bayesian approximation error approach in full-wave ultrasound tomography," IEEE Trans. Ultrason. Ferroelect. Freq. Control, **61**(10), 1627–1637 (2014).

29. Y. Xu, L. V. Wang, G. Ambartsoumian, and P. Kuchment, "Reconstructions in limited-view thermoacoustic tomography," Med. Phys., **31**(4), 724–733 (2004).

30. G. Paltauf, R. Nuster, and P. Burgholzer, "Weight factors for limited angle photoacoustic tomography," Phys. Med. Biol., **54**(11), 3303–3314 (2009).

31. A. Buehler, A. Rosenthal, T. Jetzfellner, A. Dima, D. Razansky, and V. Ntziachristos, "Model-based optoacoustic inversions with incomplete projection data," Med. Phys., **38**(3), 1694–1704 (2011).

32. K. Wang, E. Y. Sidky, M. A. Anastasio, A. A. Oraevsky, and X. Pan, "Limited data image reconstruction in optoacoustic tomography by constrained, total variation minimization," SPIE Proc. Progress in Biomedical Optics and Imaging, **7899**, 78993U(6pp) (2011).

33. C. Huang, A. A. Oraevsky, and M. A. Anastasio, "Investigation of limited-view image reconstruction in optoacoustic tomography employing a priori structural information," SPIE Proc. The International Society for Optical Engineering, **7800**, 780004(6pp) (2010).

34. M. A. Anastasio, K. Wang, J. Zhang, G. A. Kruger, D. Reinecke, and R. A. Kruger, "Improving limited-view reconstruction in photoacoustic tomography by incorporating a priori boundary information," SPIE Proc. Progress in Biomedical Optics and Imaging, **6856**, 68561B(6pp) (2008).

35. M. Xu and L. V. Wang, "Analytic explanation of spatial resolution related to bandwidth and detector aperture size in thermoacoustic or photoacoustic

reconstruction," Phys. Rev. E Stat. Nonlin. Soft Matter Phys., **67**(52), 056605(15pp) (2003).

36. M. Haltmeier and G. Zangerl, "Spatial resolution in photoacoustic tomography: Effects of detector size and detector bandwidth," Inverse Probl., **26**(12), 125002(14pp) (2010).

37. A. Rosenthal, V. Ntziachristos, and D. Razansky, "Model-based optoacoustic inversion with arbitrary-shape detectors," Med. Phys., **38**(7), 4285–4295 (2011).

38. M. L. Li, Y. C. Tseng, and C. C. Cheng, "Model-based correction of finite aperture effect in photoacoustic tomography," Opt. Express, **18**(25), 26285–26292 (2010).

39. K. Wang, S. A. Ermilov, R. Su, H. P. Brecht, A. A. Oraevsky, and M. A. Anastasio, "An imaging model incorporating ultrasonic transducer properties for three-dimensional optoacoustic tomography," IEEE Trans. Med. Imag., **30**(2), 203–214 (2011).

40. B. E. Treeby and B. T. Cox, "k-Wave: MATLAB toolbox for the simulation and reconstruction of photoacoustic wave fields," J. Biomed. Opt., **15**(2), 021314(12pp) (2010).

41. C. E. Rasmussen and C. K. I. Williams, *Gaussian Processes for Machine Learning.* (MIT Press,Cambridge, Massachusetts London, 2006).

42. X. Jin and L. V. Wang, "Thermoacoustic tomography with correction for acoustic speed variations," Phys. Med. Biol., **51**(24), 6437–6448 (2006).

43. C. Zhang and Y. Wang, "A reconstruction algorithm for thermoacoustic tomography with compensation for acoustic speed heterogeneity," Phys. Med. Biol., **53**(18), 4971–4982 (2008).

44. X. L. Den-Ben, R. Ma, D. Razansky, and V. Ntziachristos, "Statistical approach for optoacoustic image reconstruction in the presence of strong acoustic heterogeneities," IEEE Trans. Med. Imag., **30**(2), 401–408 (2011).

45. B. E. Treeby, E. Z. Zhang, and B. T. Cox, "Photoacoustic tomography in absorbing acoustic media using time reversal," Inverse Probl., **26**(11), 115003(20pp) (2010).

46. C. Huang, K. Wang, L. Nie, L. V. Wang, and M. A. Anastasio, "Full-wave iterative image reconstruction in photoacoustic tomography with acoustically inhomogeneous media," IEEE Trans. Med. Imag., **32**(6), 1097–1110 (2013).